

# Fabrication of Sectionally Permeable Components with Curved Surface by Laser-Beam Powder-Bed Fusion

Dongxu Xie<sup>1</sup>, Bernd Fränkle<sup>2</sup>, Christoph Klahn<sup>2</sup>, and Roland Dittmeyer<sup>1,\*</sup>

DOI: 10.1002/cite.202200009

 This is an open access article under the terms of the Creative Commons Attribution-NonCommercial-NoDerivs License, which permits use and distribution in any medium, provided the original work is properly cited, the use is non-commercial and no modifications or adaptations are made.

Devices in process engineering often include permeable components. As shown in our recent work for planar components, laser-beam powder bed fusion offers the opportunity to integrate permeable sections into complex monolithic metal parts in one go. This paper extends the approach to components with curved surfaces. Different scan strategies were investigated for their effects on surface morphology and permeability of tubular samples. It was found that in order to ensure consistent properties of a permeable tube, different starting points or rotation of the scan vectors have to be used.

**Keywords:** Additive manufacturing, 3D printed curved permeable material, Laser-beam powder-bed fusion, Permeable-dense composites

*Received:* January 31, 2022; *accepted:* April 27, 2022

## 1 Introduction

Laser-beam powder bed fusion (LB-PBF) is an additive manufacturing technology that directly manufactures parts by local melting of metal powder using a focused laser beam based on a sliced 3D model [1]. Porous materials produced by LB-PBF have been widely used in many applications ranging from orthopaedic implants [2] to filters [3] and gas permeable structures for injection moulding [4]. According to the fabrication principle, Stoffregen et al. classified 3D printed porous materials into two categories, namely geometrically defined lattice structure porosity (GDLSP), where the pores are basically defined by non-overlapping laser tracks, and geometrically undefined porosity (GUP), where irregular pores are generated by variation of different laser parameters [5]. Due to the smaller pore size achievable, i.e., below 100  $\mu\text{m}$ , GUP-type materials have received a lot of attention, also in process engineering. Abele et al. studied the relation between laser energy density and porosity [6]. Li et al. investigated the relation between scan speed and porosity [7]. Moreover, due to the possibility of combining porous and dense sections, permeable-dense composites based on GUP materials have been envisaged, e.g., for gas turbine combustion components [8]. Breathable mould steel is another interesting application of GUP materials. By introducing a foaming agent during the LB-PBF process, Zeng et al. were able to obtain porous materials with 2–30  $\mu\text{m}$  pore size and about 26 vol% porosity [9]. However, by laser parameter variation, GUP materials have also been made with similar pore size and porosity without a foaming agent [10]. Connecting to our previous work, where we described the

creation of permeable and dense regions in one component by LB-PBF [11], breathable moulds with integrated cooling channels made up of dense structures could be printed by LB-PBF in one go. Such moulds could reduce cooling time significantly [12].

Many potential applications of GUP materials may require components with curved surface. Zheng et al. presented a novel 3D printed structured catalyst support for use in a microreactor for methanol steam reforming [13]. In this case the GDLSP approach was used to establish well defined face-centered and body-centered cubic structures with nonporous bars. The materials enabled a high catalyst loading during subsequent coating. Combining the GDLSP and GUP approaches, hierarchical catalyst supports with porous bars in a geometrically well defined lattice structure could be made, which could offer advantages for fast reactions with high specific release or consumption of heat. In the field of membranes, Dittmar et al. presented high-performing palladium composite membranes based on tubular metallic supports. For gas-tight connection, dense tubular adapters were joined with porous membrane support tubes

<sup>1</sup>Dongxu Xie, Prof. Dr.-Ing. habil. Roland Dittmeyer  
roland.dittmeyer@kit.edu

Karlsruhe Institute of Technology (KIT), Institute for Micro Process Engineering (IMVT), Hermann-von-Helmholtz-Platz 1, 76344 Eggenstein-Leopoldshafen, Germany.

<sup>2</sup>Bernd Fränkle, Prof. Dr.-Ing. Christoph Klahn  
Karlsruhe Institute of Technology (KIT), Institute of Mechanical Process Engineering and Mechanics (MVM), Straße am Forum 8, 76131 Karlsruhe, Germany.

on both ends by laser welding [14]. However, the weld seam regions were found to be prone to form defects and cracks both in the coating of the required permeable ceramic inter-layer and of the palladium membrane similar to the planar configuration reported in our previous publication [11]. Given this, a tubular membrane support made of a permeable-dense composite in one step by LB-PBF could be an option to avoid this. However, most of the research about GUP materials is based on flat surfaces [15], and the scan strategy used for flat samples may not be suitable for curved shapes. Therefore, to the best of our knowledge, we report here for the first time the results of a systematic study into the relations between scan strategy, surface roughness, morphology, and permeability of tubular components made by LB-PBF.

## 2 Materials and Methods

### 2.1 System and Material

316L stainless steel powder (Dv (50): 31.2  $\mu\text{m}$ ) provided by Carpenter Technology Corporation (United States) and a ReaLizer SLM125 (Germany) LB-PBF machine were used in this study.

As shown in Fig. 1, tubes (diameter 30.2 mm, wall thickness 2 mm, height 20 mm) were printed for investigating the effects of the scanning strategy on the properties of the resulting components. The relevant parameters including hatch distance, layer thickness, and scanning direction can be controlled by the ReaLizer SLM125 operating system. In this study, all samples were printed with the same parameters: laser power was 80 W, hatch distance was 0.1 mm, layer thickness was 50  $\mu\text{m}$ , laser spot size was 50  $\mu\text{m}$ , and scan speed was 1000  $\text{mm s}^{-1}$ . Four surfaces (front, back, left, right) relative to the scanning direction were marked for the isotropy study. Samples with 0.14 mm hatch distance were prepared for permeability measurements. In order to avoid the influence of boundary tracks on the porous surface, all samples were printed without outer and inner boundary scanning.

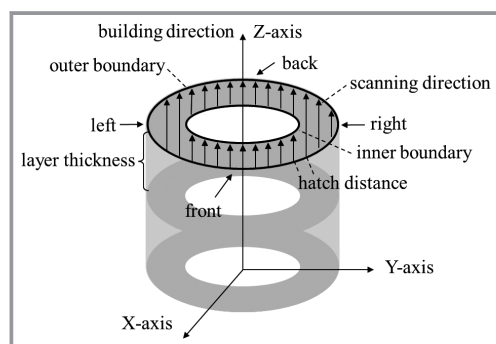


**Figure 1.** Overview of scanning parameters for tubular samples.

### 2.2 Determination of Porosity

The porosity was calculated following Eq. (1).

$$\varepsilon = \left( 1 - \frac{m_t \rho_{\text{met}}^{-1}}{V_t} \right) \cdot 100\% \quad (1)$$

with  $V_t = \pi(r_o^2 - r_i^2)h_t$ .  $m_t$  is the mass of the permeable tube, and each individual sample was weighed by a precision balance ( $\pm 1$  mg),  $\rho_{\text{met}}$  is the bulk density of the metal (316L stainless steel, 8  $\text{g cm}^{-3}$  [16]),  $r_o$ ,  $r_i$ ,  $h_t$  denote the outer radius, inner radius, and height of the tube, respectively. The dimensions of the tube were given in a CAD model ( $r_o = 15.1$  mm,  $r_i = 13.1$  mm,  $h_t = 20$  mm).

### 2.3 Determination of Roughness and Morphology

The surface roughness (arithmetic mean height of the surface: Sa) and surface 3D profile were studied by a 3D optical profiler (S-neox, Sensofar with ISO 25178). Micrographs were taken by a scanning electron microscope (SEM, JSM 6300, Jeol with a 10 kV beam).

### 2.4 Permeability Measurements

As shown in Fig. 2, a standard pressure nutsch according to VDI Guideline 2762 [17], typically used for filter characterization, was used to determine the permeability of tubular

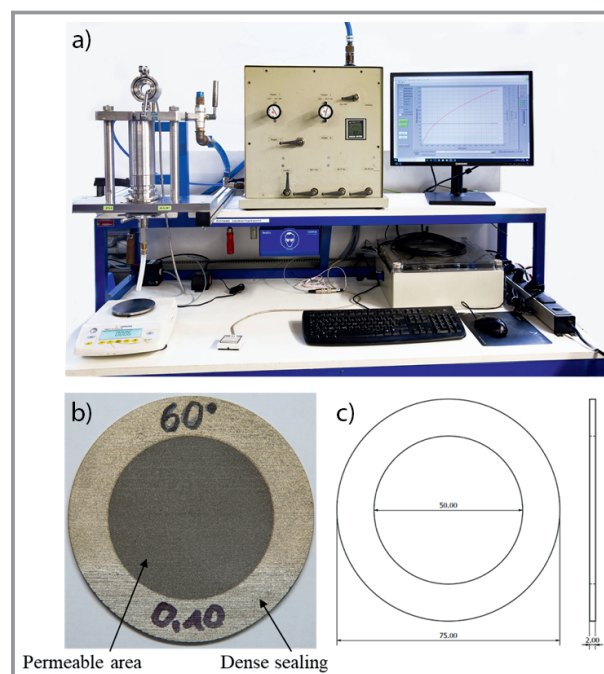


**Figure 2.** Permeability testing. a) Pressure nutsch for measuring the permeation flux, b) permeable sample, c) schematics of a permeable sample.

components made with unidirectional scan vectors (USV) of different direction as wells as with rotated scan vectors (RSV). As the unit does not accept tubular samples, flat disk-shaped samples with a circular permeable area of 50 mm in diameter were printed with the same parameters and in the same orientation in the build volume like the permeable tubes.

The definition of permeability is based on the D'Arcy equation given in Eq. (2). Tests were done by gravimetrically measuring the permeate accumulation rate  $\dot{m}$  of a laminar flow of deionized water through a permeable tube, and by neglecting friction.

$$K = \frac{\dot{m}}{A} \frac{h}{\rho_{\text{Fluid}}} \frac{\eta_{\text{Fluid}}}{\Delta p} \quad (2)$$

### 3 Results and Discussion

#### 3.1 Permeable Tubes Printed with Unidirectional Scan Vectors

Fig. 3 shows the schematics of a permeable tube printed by USV. In our previous research we found that flat permeable samples printed by USV showed smaller surface roughness than for other scanning strategies [11]. However, samples with curved surface printed by USV had not been studied.

As shown in Fig. 4a, a staircase structure appeared on the left surface of the sample. From the magnified image, the appearance of the staircase structure in  $x$ - and  $y$ -direction is highly related to the orientation of the surface of the sample. When the sample surface is parallel to the scan direction, the staircase structures are more visible. As shown in Fig. 4b, there were no staircase structures on the front surface of the sample. Since the front surface of the sample is composed of the starting point of the vectors, and the left surface of the sample is composed of the sides of the vectors, the permeable tube shows different surface morphology at different positions.

Figs. 5a and 5b show the front and back surface of permeable tubes printed by USV. The front surface is composed of the initial points of the scan vectors and the back surface is composed of the terminal points. Since the positions of the scan vectors in every layer are always the same, stripes formed by the initial points of the vectors in the same position can be seen in Fig. 5a. During the printing process, the powder shrinks with laser scanning. Therefore, there is less powder at the terminal points compared to the initial points of the vectors. As visible from Figs. 5a and 5b, the back surface exhibits more defects than the front surface, resulting from a lack of powder.

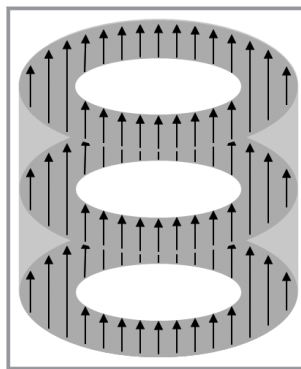


Figure 3. Schematic of a scan strategy with unidirectional scan vectors (USV) to produce a permeable tube.

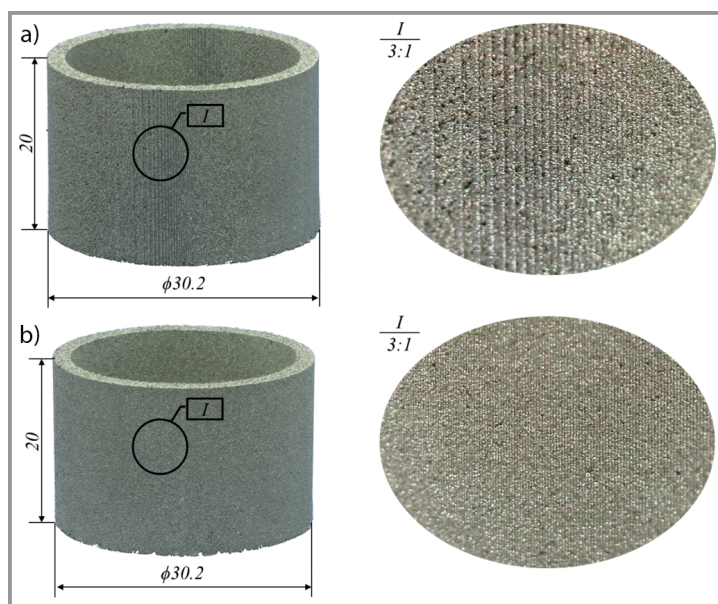


Figure 4. Permeable tube produced by a unidirectional scan vector (USV) strategy. a) Left surface, b) front surface.

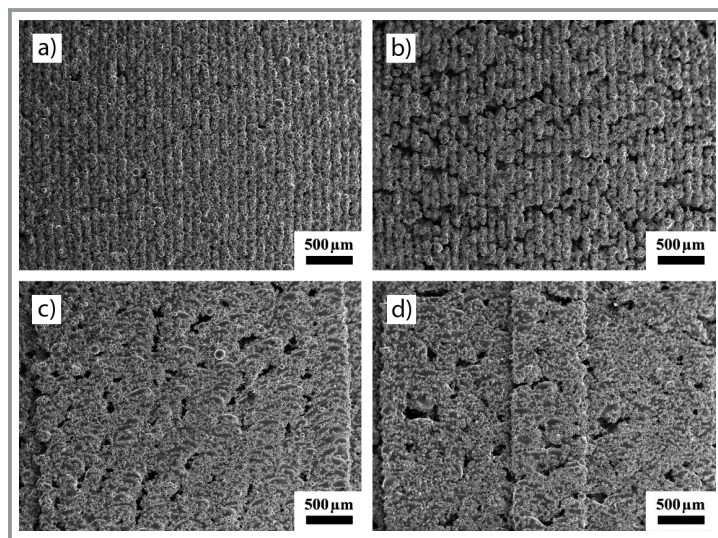


Figure 5. Curved surfaces emerging from a unidirectional scan vector (USV) strategy. a) Front surface, b) back surface, c) left surface, d) right surface.

Figs. 5c and 5d show the left and right surfaces of a permeable tube printed by USV. Both surfaces are composed of the sides of the scan vectors. During laser scanning, not fully melted powder in the laser tracks causes defects on the left and right surface, while porous structures in the front surface are formed by gaps between individual tracks. The morphology of these two kinds of pores in the curved surface here is similar to the one found in flat samples in previous research [11]. As visible from Fig. 5, with USV, the porous structures on the permeable tube are anisotropic. Moreover, the precision of the left and right surface is limited by the laser track thickness as there are step structures on the left and right surface.

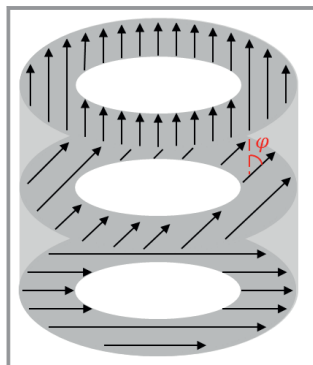
The porosity of the permeable tube shown in Figs. 4 and 5 is 25.3%. As to be seen from Tab. 1, the roughness of the tube is anisotropic as well. It is lowest at the front surface compared to the other surfaces. Owing to defects and staircase structures on the surface, the roughness of the left and right surface is higher compared to that of the front surface. Lack of powder at the terminal points of the scan vectors causes the roughness of the back surface to be higher than that of the front surface.

**Table 1.** Roughness of different surfaces of permeable tubes printed with a scan strategy based on unidirectional scan vectors (USV).

Surface	Roughness [ $\mu\text{m}$ ]
Front	$27.3 \pm 4.2$
Back	$35.4 \pm 1.6$
Left	$33.4 \pm 2.5$
Right	$33.8 \pm 2.1$

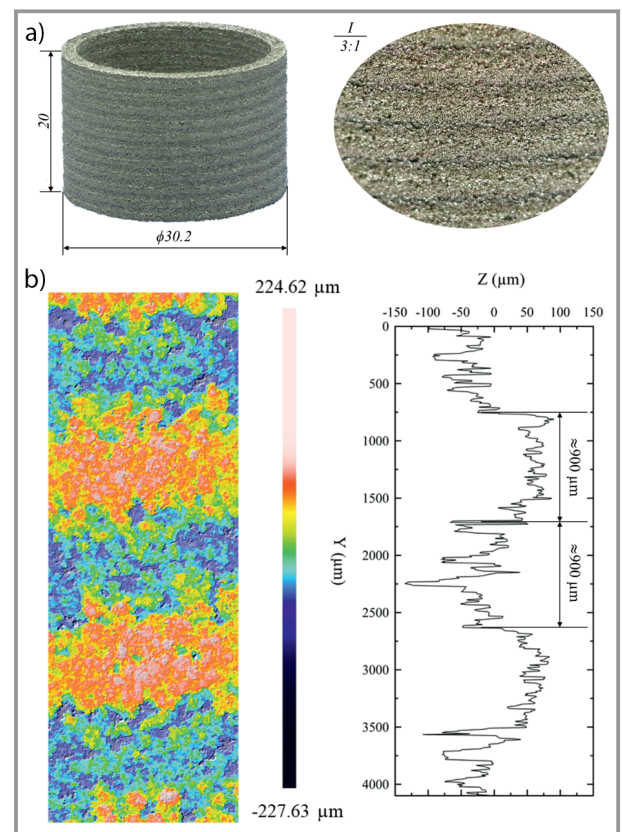
### 3.2 Permeable Tubes Printed with Rotated Scan Vectors

To obtain a permeable tube with an isotropic porous structure on the surface, a permeable tube with rotated scan vectors was printed. Fig. 6 shows the schematic of this scan strategy. Different rotation angles between adjacent layers can be set in the Realizer SLM125 operating system.



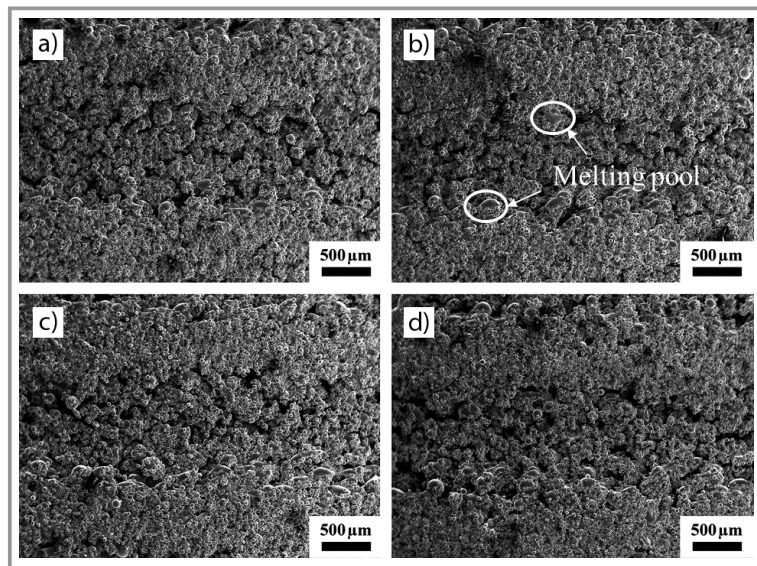
**Figure 6.** Schematic of a scan strategy based on rotated scan vectors (RSV) to produce a permeable tube.

Fig. 7a shows a permeable tube made with rotated scan vectors using an angle of rotation of  $10^\circ$ . Clearly, the tube surface is composed of two spirals. As shown in Fig. 7b, the thicknesses of both spirals is around  $900 \mu\text{m}$ . Since the layer thickness during printing was set to  $50 \mu\text{m}$ , every  $1800 \mu\text{m}$  the scan vector will come back to the initial scanning direction. This distance is equal to the combined thickness of the two superimposed spirals. The thickness of the spirals is highly related to the angle of rotation. The reason of the spiral structure on the surface is that one spiral is composed of the initial points of the scan vectors whereas the other one is composed of the terminal points of the scan vectors. Therefore, the thicknesses of the two spirals are the same.



**Figure 7.** a) Permeable tube printed with a scan strategy based on rotated scan vectors (RSV) and an angle of rotation of  $10^\circ$ ; b) surface roughness profile of this tube.

Fig. 8 provides SEM pictures of the front, back, left and right surfaces, respectively, of the permeable tube shown in Fig. 7. The morphology of permeable tubes printed with the RSV scan strategy is apparently isotropic. No significant differences can be identified in the SEM pictures from the front, back, left, and right surface. Melting pools can be seen on the boundary of the two spirals. As shown in Figs. 5c and 5d, when the scan vectors are parallel to the surface, melting pools appear on the surface. Therefore, the boundary of the two spirals is also the boundary of the initial points and the terminal points of the scan vectors. This is



**Figure 8.** Curved surfaces on a permeable tube produced with rotated scan vectors (RSV) and an angle of rotation of 10°. a) Front surface, b) back surface, c) left surface, d) right surface.

consistent with the explanation of the spirals given in the context of Fig. 7.

The porosity of the permeable tube printed with 10° RSV is 22.8%. With the same laser power, the permeable tube printed with RSV has a lower porosity compared to the permeable tube printed by USV. Tab.2 lists the measured roughness of the different surfaces of the tube shown in Fig. 7. Due to the spiral structures on the surface, the roughness is higher than for printing with USV, but similar values are obtained for all four surfaces.

**Table 2.** Roughness of the different surfaces of a permeable tube produced by rotated scan vectors (RSV) with an angle of rotation of 10°.

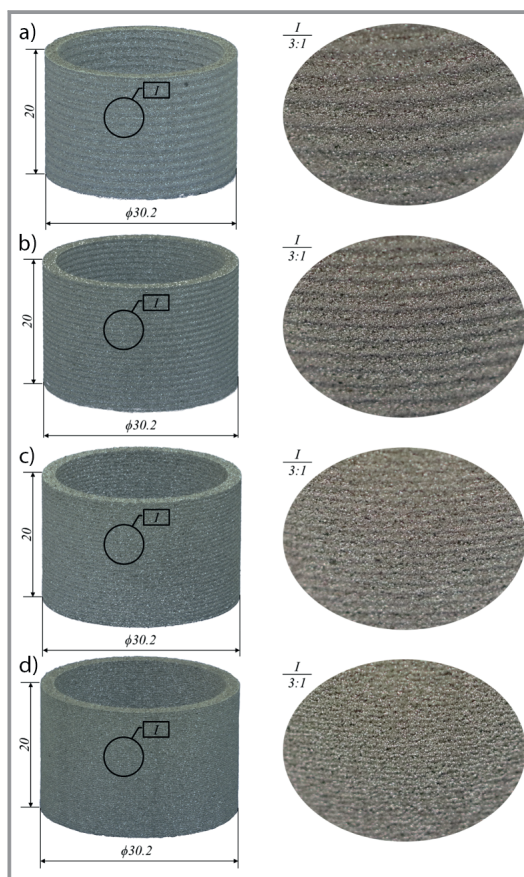
Surface	Roughness [ $\mu\text{m}$ ]
Front	$47.6 \pm 0.9$
Back	$44.7 \pm 0.8$
Left	$44.0 \pm 1.6$
Right	$45.2 \pm 1.7$

Fig. 9 shows permeable tubes printed with the RSV scan strategy and different angle of rotation. All samples have spiral structures on the surface. When the angle of rotation is 12°, 20°, 30°, 60°, every 1500  $\mu\text{m}$ , 900  $\mu\text{m}$ , 600  $\mu\text{m}$ , and 300  $\mu\text{m}$  the scan vectors will come back to the initial position, respectively. Therefore, as shown in Fig. 8, with increasing rotation angle, the slope of the spirals is decreasing.

Fig. 10 shows the SEM pictures of the tubes printed with 12° RSV, 20° RSV, 30° RSV, and 60° RSV, respectively. The

slope of the spiral meets the previous expectations, which indicates that the spiral structure can be controlled by the angle of rotation. Moreover, melting pools were found on the surface of all samples. This reinforces the explanation that the two spiral structures on the tube surface are composed of the initial points and terminal points of the individual scan vectors.

As shown in Tab.3, the permeable tube printed with 60° RSV shows the lowest porosity compared to all other samples. All samples printed with RSV have lower porosity compared to permeable tubes printed with USV. The roughness of permeable tubes printed with RSV is higher than the roughness of the front surface of permeable tubes printed with USV. The main reason is that the spiral structures typical of RSV increase the roughness of the permeable tube. Another reason is that the spirals are composed of the initial and terminal points of the vectors. As shown in Table 1, the surface composed of the terminal points of the vectors has a higher roughness compared to the surface composed of



**Figure 9.** Permeable tubes produced with rotated scan vectors (RSV) and different angle of rotation. a) 12° RSV, b) 20° RSV, c) 30° RSV, d) 60° RSV.

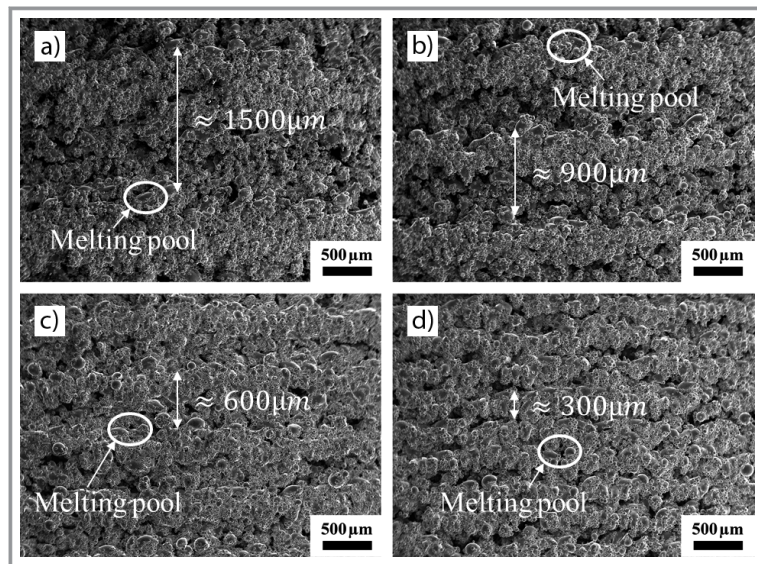


**Figure 10.** Curved surfaces of permeable tubes printed with rotated scan vectors (RSV) and different angle of rotation. No more distinction between front, back, left and right surface. a) 12° RSV, b) 20° RSV, c) 30° RSV, d) 60° RSV.

the initial points of the vectors. The roughness of RSV-printed permeable tubes decreases with an increase of the angle of rotation. The reason is that the slope of the spirals decreases with higher angle of rotation. As shown in Fig. 10 (d), the reduced slope of the spirals makes the surface of the permeable tube printed with 60° RSV smoother than those of the other ones printed with lower angle of rotation.

**Table 3.** Porosity and surface roughness of permeable tubes printed with rotated scan vectors (RSV) and different angle of rotation.

Rotation angle	Porosity [%]	Roughness [ $\mu\text{m}$ ]
12°	21.9	45.4 $\pm$ 4.2
20°	22.0	44.9 $\pm$ 2.8
30°	22.0	44.7 $\pm$ 1.1
60°	20.6	38.7 $\pm$ 2.2

### 3.3 Permeable Tubes Printed by Four Direction Scan Vectors

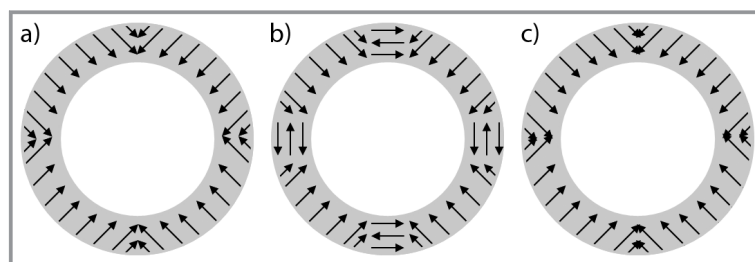
Another scan strategy is to use four direction scan vectors (FDSV). Fig. 11a shows the schematic of this approach. The four directions are at right angles to each other, namely 45°, 135°, 225° and 315°. Two variants of this strategy have been pursued as well. Fig. 11b shows the schematic of an FDSV approach combined with connection scan vectors (FDCSV). This scanning strategy uses four direction vectors and the scan vectors in different directions are connected by

1 mm long connection vectors. Fig. 11c shows a different way of connecting the four direction scan vectors. This is called four direction overlap scan vectors (FDOSV), and 0.5 mm overlap is realized between the scan vectors in different directions.

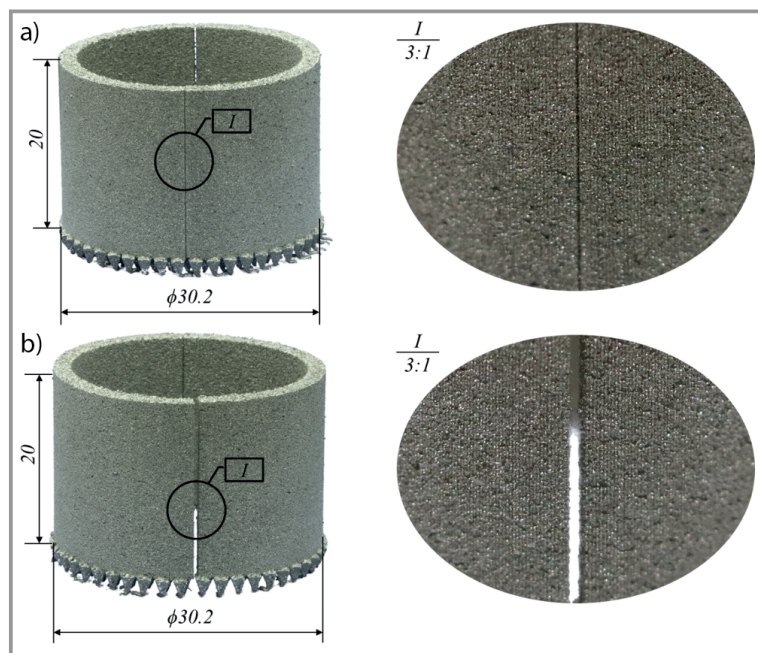
Fig. 12a shows the permeable tube printed with the FDSV strategy. There is an obvious gap between the scan vectors in different directions. As shown in Fig. 12a, the area near the gap is composed of the terminal points of the scan vectors. The lack of powder at the terminal points of the vectors is one reason for gap formation. In addition, the position of the terminal points of the vectors in different directions may not have matched perfectly. As shown in Fig. 12b, the parts printed with different scan vector directions are not combined to one piece. In turn, the permeable tube printed with this scanning strategy cannot be separated from the supporting structures or other fixed structures and exist on its own.

For comparison, Fig. 13a shows the permeable tube printed with the FDOSV strategy. A groove created by the connection vectors can be observed between the permeable parts printed by the scan vectors in different directions. As shown in Fig. 13b, the thickness of this groove is around 100  $\mu\text{m}$ . There is a 200  $\mu\text{m}$  gap at the right side of the groove. This may be due to the fact that the direction of adjacent connection vectors was altered by 180°, respectively. The first vector on the surface is printed from left to right. Since the terminal point lacks powder and the position may not match perfectly, a gap emerged on the right of the groove. While the second vector was printed from right to left and the hatch distance was 100  $\mu\text{m}$ . Therefore, the thickness of the gap is 200  $\mu\text{m}$ .

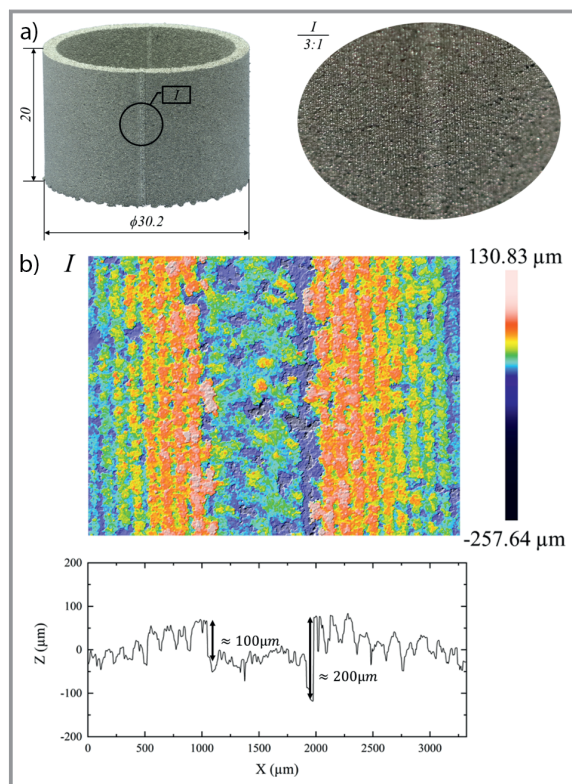
Fig. 14a shows the permeable tube printed with the FDOSV strategy. There is an overlap area between the scan vectors in different directions. Since the overlap area forms from more initial points of the individual scan vectors, there is no stripe structure to be seen in the overlap area in Fig. 14 b. It can be observed from the roughness profile that there is neither a convex nor a concave structure in the overlap area and the transition is rather smooth.



**Figure 11.** Schematics of three different four direction scan strategies, a) FDSV, b) FDCSV, c) FDOSV.



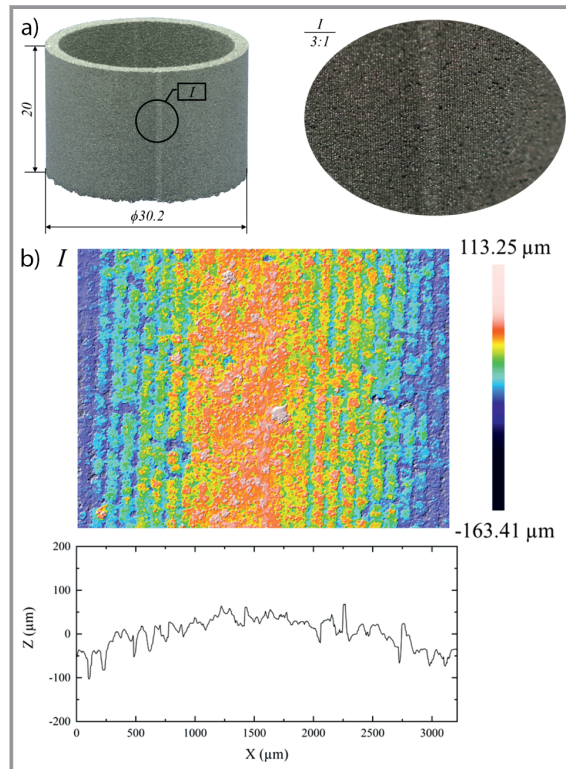
**Figure 12.** a) Permeable tube printed by a scan strategy based on four (orthogonal) direction scan vectors (FDSV), b) gap between scan vectors in different directions.



**Figure 13.** a) Permeable tube printed by a scan strategy based on four direction scan vectors and additional connection vectors (FDCSV), b) surface roughness profile of the tube surface showing a groove in the connection area.

The roughness of the permeable tube printed with the FDOSV strategy was measured from four directions. As shown in Tab. 4, with around 28  $\mu\text{m}$  in all four directions, the surface roughness is substantially lower than for the RSV scan strategy. Moreover, compared to permeable tubes printed by USV, the roughness of the permeable tube printed by FDOSV is isotropic.

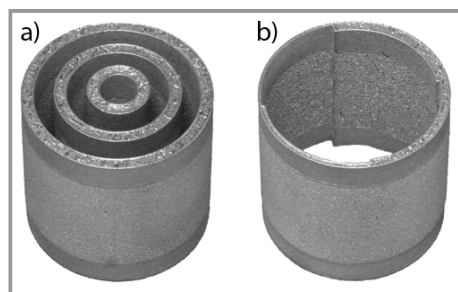
Fig. 15a shows permeable-dense tubes with 30 mm, 20 mm, and 10 mm outer diameters printed with the FDOSV scan strategy. The height of the permeable part is 2 mm, and the wall thickness of all tubes is 2 mm. On the bottom and top of the permeable tube, 5 mm dense structures were printed. In addition, Fig. 15b shows a permeable-dense tube with 0.5 mm, 1 mm, 1.5 mm, and 2 mm wall thickness, as well printed with the FDOSV scan strategy. Here, the outer diameter of the permeable part is 30 mm, and the height of the permeable part is 20 mm. On the bottom and top of the permeable tube, 5 mm dense structures were printed. As visible from Figs. 15a and 15b, with the FDOSV scan strategy permeable parts with curved surfaces can be printed in different diameters and thicknesses. Moreover, permeable parts and dense parts can be freely combined.



**Figure 14.** a) Permeable tube printed by FDOSV, b) 3D profile of permeable tube printed by FDOSV.

**Table 4.** Roughness of different surfaces of permeable tube printed by four direction overlap vectors.

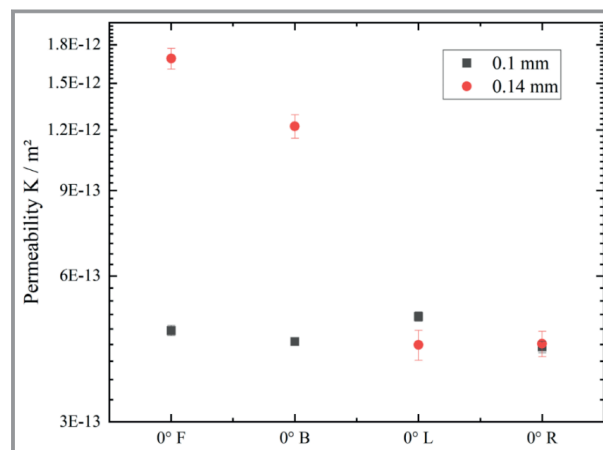
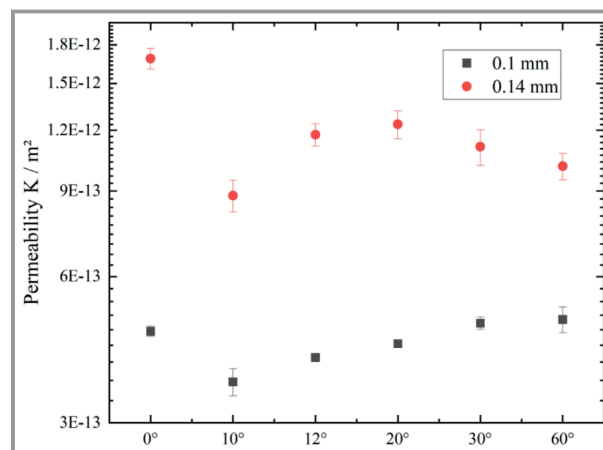
Surface	Roughness [ $\mu\text{m}$ ]
Front	$27.6 \pm 0.9$
Back	$28.9 \pm 1.4$
Left	$27.4 \pm 1.2$
Right	$27.9 \pm 1.1$

**Figure 15.** Demonstration of the suitability of the FDOVS scan strategy for printing of permeable-dense components with curved surfaces. a) Tubes with 30 mm, 20 mm, 10 mm height and 2 mm wall thickness each. Height of the permeable part 20 mm, height of the dense parts 5 mm. b) 30 mm  $\times$  30 mm tube with four different wall thicknesses staggered 90°-wise, i.e., 0.5 mm, 1 mm, 1.5 mm, 2 mm.

### 3.4 Permeability Results

For an application of 3D printed permeable tubes in, e.g., filtration, it is important that the tube's properties are consistent. The permeability according to Eq. (2) is an important parameter from a process engineering point of view and it allows verification of the effects of the fabrication process on the performance of the components. Fig. 16 provides the permeability of tubes in different directions, i.e., front, back, left and right, for 0.10 mm and 0.14 mm hatch distance. The tubes were made with the USV scan strategy. For a small hatch distance of 0.1 mm, the permeability is small so that differences in the morphology among the four different sides of the tube do not result in different values of the measured permeability. A larger hatch distance of 0.14 mm leads to a different behavior. Here the permeability in the front and on the back side is about three times as high as on the left and right side, where the permeability is in the same range as for 0.10 mm hatch distance.

Furthermore, permeability measurements were executed on tubes printed with the RSV scan strategy and different angle of rotation. Fig. 17 shows the results for an angle of rotation between 10° and 60°. The permeability of the front surface of the permeable tube printed with the USV scan strategy is given at 0° as a reference. Like for the USV scan strategy, the permeability of tubes made with the RSV strategy decreases with lower hatch distance. The angle of rotation shows a moderate influence on permeability. While it seems to increase moderately with increasing angle of rota-

**Figure 16.** Permeability of different sides of permeable tubes printed with the USV scan strategy and hatch distances of 0.10 mm and 0.14 mm, respectively. Note that measurements were performed with flat samples printed with the same parameters and in the same orientation in the build volume like the tubular samples. 0° F stands for front side, 0° B for the back side, 0° L for the left side, and 0° R for the right side. Error bars mark the standard deviation of the permeability measurements.**Figure 17.** Permeability of tubes made with the RSV scan strategy and different angle of rotation for two different hatch distances, i.e., 0.10 mm and 0.14 mm. Values at 0° denote the front surface of a tube made with the USV strategy. Error bars denote the standard deviation of the permeability measurements.

tion for small hatch distance, larger hatch distance leads to a weak maximum at 20° angle of rotation.

Summarizing, it can be stated that with increasing hatch distance, which is needed for highly permeable structures, more advanced scan strategies than USV have to be considered to ensure that the permeability will be independent of the perimeter direction.

## 4 Conclusions

In this study, different scanning strategies have been analyzed for 3D printing of permeable components with curved surfaces. Permeable tubes printed with unidirectional scan vectors (USV) clearly show anisotropy of the surface morphology. The front surface formed by the initial points of the scan vectors has the lowest roughness compared to the other surfaces. The back surface formed by the terminal points of the scan vectors shows defects. The left and right surfaces made up by the sides of the scan vectors have staircase structures. Permeable tubes printed by rotated scan vectors (RSV) show isotropy of the surface morphology. Two spiral structures composed of the initial and the terminal points of the scan vectors can be observed on the surface. The slope of the spirals is highly related to the angle of rotation of the scan vectors. Permeable tubes printed with 60° RSV have shown the smallest slope and the lowest roughness compared to all other permeable tubes printed with the RSV scan strategy. Permeable tubes printed by four direction scan vectors (FDSV) without connecting vectors or overlap show gaps between the different parts corresponding to the directions of the scan vectors. Adding connection vectors (FDCSV) enables the fabrication of coherent tubes but leads to grooves between the scan vectors in different directions. Finally, permeable tubes printed by four direction scan vectors with overlap (FDOSV) show isotropic properties and lower surface roughness compared to permeable tubes printed with the RSV scan strategy. Based on this research, permeable-dense tubes with different outer diameter and wall thickness can be fabricated reliably with the FDOSV scan strategy. Furthermore, permeability measurements have shown that rotated scan vectors or multiple direction scan vectors should be used above a certain hatch distance to ensure uniform tube properties.

This research was supported by the Chinese Scholarship Council (fellowship to D. Xie). The authors would like to thank Mr. Florian Messerschmidt from IMVT (KIT) for taking the SEM pictures. Open access funding enabled and organized by Projekt DEAL.

## Abbreviations

LB-PBF	Laser-beam powder bed fusion
GDLSF	Geometrically defined lattice structure porosity
GUP	Geometrically undefined porosity
SEM	Scanning electron microscopy
USV	Unidirectional scan vectors
RSV	Rotated scan vectors
FDSV	Four direction scan vectors
FDCSV	Four direction vectors and connection scan vectors
FDOSV	Four direction overlap scan vectors

## References

- [1] V. Bhavar, P. Kattire, V. Patil, S. Khot, K. Gujar, R. Singh, A review on powder bed fusion technology of metal additive manufacturing, in *Additive manufacturing handbook: Product development for the Defense industry* (Eds: A. B. Badiru, V. V. Valencia, D. Liu), 1st ed., CRC Press, Boca Raton, FL **2017**, 251–253.
- [2] L. Wang, J. Kang, C. Sun, D. Li, Y. Cao, Z. Jin, Mapping porous microstructures to yield desired mechanical properties for application in 3D printed bone scaffolds and orthopaedic implants, *Mater. Des.* **2017**, *133*, 62–68. DOI: <https://doi.org/10.1016/j.matdes.2017.07.021>
- [3] I. Yadroitsev, I. Shishkovsky, P. Bertrand, I. Smurov, Manufacturing of fine-structured 3D porous filter elements by selective laser melting, *Appl. Surf. Sci.* **2009**, *255*, 5523–5527. DOI: <https://doi.org/10.1016/j.apsusc.2008.07.154>
- [4] C. Klahn, F. Bechmann, S. Hofmann, M. Dinkel, C. Emmelmann, Laser Additive Manufacturing of Gas Permeable Structures, *Phys. Procedia* **2013**, *41*, 873–880. DOI: <https://doi.org/10.1016/j.phpro.2013.03.161>
- [5] H. Stoffregen, J. Fischer, C. Siedelhofer, E. Abele, Selective laser melting of porous structures, *Solid Freeform Fabr. Symp. Proc.* **2011**, 680–695.
- [6] E. Abele, H. A. Stoffregen, M. Kniepkamp, S. Lang, M. Hampe, Selective laser melting for manufacturing of thin-walled porous elements, *J. Mater. Process. Technol.* **2015**, *215*, 114–122. DOI: <https://doi.org/10.1016/j.jmatprotec.2014.07.017>
- [7] R. Li, J. Liu, Y. Shi, M. Du, Z. Xie, 316L Stainless Steel with Gradient Porosity Fabricated by Selective Laser Melting, *J. Mater. Eng. Perform.* **2010**, *19*, 666–671. DOI: <https://doi.org/10.1007/s11665-009-9535-2>
- [8] A. Graichen, J. Larfeldt, D. Lörst, E. Munktel, Porous rotating machine component, combustor and manufacturing method, *U.S. Patent 10,753,609*, **2020**.
- [9] G. H. Zeng, T. Song, Y. H. Dai, H. P. Tang, M. Yan, 3D printed breathable mould steel: Small micrometer-sized, interconnected pores by creatively introducing foaming agent to additive manufacturing, *Mater. Des.* **2019**, *169*, 107693. DOI: <https://doi.org/10.1016/j.matdes.2019.107693>
- [10] S. Guddati, A. S. K. Kiran, M. Leavy, S. Ramakrishna, Recent advancements in additive manufacturing technologies for porous material applications, *Int. J. Adv. Manuf. Technol.* **2019**, *105*, 193–215. DOI: <https://doi.org/10.1007/s00170-019-04116-z>
- [11] D. Xie, R. Dittmeyer, Correlations of laser scanning parameters and porous structure properties of permeable materials made by laser-beam powder-bed fusion, *Addit. Manuf.* **2021**, 102261. DOI: <https://doi.org/10.1016/j.addma.2021.102261>
- [12] S. A. Jahan, T. Wu, Y. Zhang, J. Zhang, A. Tovar, H. El-Mounayri, Effect of Porosity on Thermal Performance of Plastic Injection Molds Based on Experimental and Numerically Derived Material Properties, in *Mechanics of Additive and Advanced Manufacturing*, Volume 9, Springer International Publishing, Cham **2018**, 55–63.
- [13] T. Zheng, W. Zhou, D. Geng, Y. Li, Y. Liu, C. Zhang, Methanol steam reforming microreactor with novel 3D-Printed porous stainless steel support as catalyst support, *Int. J. Hydrogen Energy* **2020**, *45*, 14006–14016. DOI: <https://doi.org/10.1016/j.ijhydene.2020.03.103>
- [14] B. Dittmar, A. Behrens, N. Schödel, M. Rüttinger, T. Franco, G. Straczewski, R. Dittmeyer, Methane steam reforming operation and thermal stability of new porous metal supported tubular palladium composite membranes, *Int. J. Hydrogen Energy* **2013**, *38*, 8759–8771. DOI: <https://doi.org/10.1016/j.ijhydene.2013.05.030>

- [15] T. Furumoto, A. Koizumi, M. R. Alkahari, R. Anayama, A. Hosokawa, R. Tanaka, T. Ueda, Permeability and strength of a porous metal structure fabricated by additive manufacturing, *J. Mater. Process. Technol.* **2015**, *219*, 10–16. DOI: <https://doi.org/10.1016/j.jmatprotec.2014.11.043>
- [16] J. Suryawanshi, K. G. Prashanth, U. Ramamurty, Mechanical behavior of selective laser melted 316L stainless steel, *Mater. Sci. Eng., A* **2017**, *696*, 113–121. DOI: <https://doi.org/10.1016/j.msea.2017.04.058>
- [17] VDI 2762 Blatt 2, *Mechanical solid-liquid separation by cake filtration Mechanical solid-liquid separation by cake filtration – Determination of filter cake resistance*, VDI-Verlag, Dusseldorf **2010**. [www.vdi.de/en/home/vdi-standards/details/vdi-2762-blatt-2-mechanical-solid-liquid-separation-by-cake-filtration-determination-of-filter-cake-resistance](http://www.vdi.de/en/home/vdi-standards/details/vdi-2762-blatt-2-mechanical-solid-liquid-separation-by-cake-filtration-determination-of-filter-cake-resistance)